



Catalytic aqueous CO₂ reduction to formaldehyde at Ru surface on hydroxyl-groups-rich LDH under mild conditions

Lidan Deng^a, Zheng Wang^b, Xingmao Jiang^c, Jie Xu^a, Zijian Zhou^a, Xiaozhong Li^d, Zhixiong You^d, Mingyue Ding^e, Tetsuya Shishido^f, Xiaowei Liu^{a,1,*}, Minghou Xu^a

^a State Key Laboratory of Coal Combustion, Huazhong University of Science and Technology, 1037 Luoyu Road, Wuhan 430074, PR China

^b Research Center for Eco-Environmental Sciences, Chinese Academy of Sciences, 18 Shuangqing Road, Haidian District, Beijing 100085, PR China

^c School of Chemical Engineering and Pharmacy, Wuhan Institute of Technology, 206, Guanggu 1st road, Donghu New & High Technology Development Zone, Wuhan 430205, PR China

^d School of Resources and Environmental Sciences, Wuhan University, 299 Bayi Road, Wuchang District, Wuhan 430079, PR China

^e School of Power and Mechanical Engineering, Wuhan University, 299 Bayi Road, Wuchang District, Wuhan 430079, PR China

^f Department of Applied Chemistry for Environment, Graduate School of Urban Environmental Sciences, Tokyo Metropolitan University, 1-1 Minami-Osawa, Hachioji, Tokyo 192-0397, Japan

ARTICLE INFO

Keywords:

Carbon dioxide
Formaldehyde
Layered double hydroxide
Hybrid electronic state
Ru

ABSTRACT

Various value-added chemicals such as formic acid, carbon monoxide, methane, methanol, have been obtained using CO₂ as a feedstock. However, formaldehyde generation from CO₂ is less reported. Here, we performed CO₂ hydrogenation with H₂ in additive-free water and used layered double hydroxide supported Ru as the heterogeneous catalyst. It was found that gaseous CO₂ and H₂ could be efficiently and selectively converted to formaldehyde dissolved in water even at room temperature with ambient pressure. The highest gaseous CO₂ conversion of 89.7% and a formaldehyde yield of 58.7% were achieved using a Ru/LDH-red catalyst in water at 30 °C with 10 bar CO₂ and 10 bar H₂. Combined with experimental and theoretical studies, HCOOH was found as the important reaction intermediate. The rich surface -OH of LDH and hybrid electronic state of Ru over Ru/LDH-red catalyst resulted in highly efficient HCHO formation. Our findings offer opportunities to one energy-efficient formaldehyde synthesis method.

1. Introduction

The utilization of carbonaceous fuels (coal, petroleum, and natural gas) for energy generation has led to exponential progress of human civilization, while also resulted in a tremendous amount of CO₂ emission. The current > 400 ppm of CO₂ concentration in the atmosphere is building enormous pressure on the natural carbon cycle, and affecting almost all sectors in human-being society. Global warming, climate change, ocean acidification have become major public issues. Great efforts have been made to mitigate CO₂ emission, among which converting CO₂ to chemical products sustainably is the ideal solution [1–8]. Some single carbon (C₁) products such as formic acid [9,10], carbon monoxide [11–16], methane [17–19] and methanol [20–25] have been reported using CO₂ as the feedstock. However, the synthesis of another important C₁ product, formaldehyde (HCHO), via CO₂ hydrogenation is much less

investigated.

HCHO is a crucial ingredient and key building block in more than 50 industries such as resins, polymers, cosmetics, adhesives and paints in our society. The annual production of HCHO over the world is recently over 30 megatons [26,27]. As a highly versatile platform chemical, HCHO is industrially produced through three stages (the formox process): (a) steam reforming of natural gas to syngas, (b) methanol (CH₃OH) synthesis and (c) partial oxidation of CH₃OH to HCHO (Supplementary Table S1) [28]. After more than a century since 1882, the formox process is still the leading technology and produces the majority of total global HCHO. However, large units for combustion, compression and purification and all high temperature reactions in this process are energy-intensive, leading to high economic costs and ecological deficiencies. A more environmentally friendly and efficient route for HCHO production is crucially needed for a sustainable society.

* Corresponding author.

E-mail address: xwliu@hust.edu.cn (X. Liu).

¹ <https://orcid.org/0000-0003-3970-1309>.

<https://doi.org/10.1016/j.apcatb.2022.122124>

Received 31 July 2022; Received in revised form 30 September 2022; Accepted 26 October 2022

Available online 29 October 2022

0926-3373/© 2022 Elsevier B.V. All rights reserved.

HCHO formation was once observed in gas-phase CO₂ hydrogenation at 150 °C and 6 bar using a PtCu/SiO₂ heterogeneous catalyst [29] or a NiCo catalyst at 200 °C and 6 bar [30]. However, the CO₂ conversions were below 1% and byproducts such as CO, CH₃OH were also formed. Indeed, the hydrogenation of CO₂ to HCHO by H₂ in gas-phase reactions is thermodynamically unfavorable, as it is a strongly endothermic reaction at ambient conditions (CO₂ (g) + 2 H₂ (g) → HCHO (g) + H₂O (g) $\Delta H^0 = 39.8 \text{ kJ}\cdot\text{mol}^{-1}$). In 2015, Tanksale and co-workers first reported a promising approach based on the conversion of syngas (CO + H₂) to HCHO in the aqueous phase [31,32]. Although gas-phase hydrogenation of CO by H₂ for HCHO production is also thermodynamically unfavored and affords low yields (<0.2%), performing it in liquid rather than in the gaseous phase causes the reaction to become thermodynamically favored. 19.14% of CO conversion and 100% of a selectivity toward HCHO were obtained using a Ru-Ni/Al₂O₃ catalyst in water at 80 °C and 100 bar [31]. This successful conversion in the liquid phase opens up a new opportunity toward a more efficient and sustainable HCHO production route because it results in high activity and selectivity toward HCHO at low temperatures. Tanksale et al. further converted CO₂, a more attractive feedstock, into HCHO using a Pt-Ni/Al₂O₃ heterogeneous catalyst. However, even under 70 bar of total pressure with 16 of H₂/CO₂ ratio, the equilibrium HCHO yield over the catalyst was only 1.8 mmol·L⁻¹·g cat⁻¹ at 25 °C [33].

In this work, we report a much more active heterogeneous catalyst, a layered double hydroxide (LDH)-supported ruthenium (Ru) catalyst for HCHO production via liquid-phase hydrogenation of CO₂. The highest HCHO yield of 583 mmol·L⁻¹·gcat⁻¹ and high selectivity toward HCHO were achieved at 30 °C with 10 bar of CO₂ and 10 bar of H₂ in water without any additives. This activity is about 200 times higher than the value reported in the literature mentioned above under much milder conditions. Gaseous CO₂ and H₂ at ambient pressure even can be efficiently converted to HCHO dissolved in water at low temperature (18 °C). This work expands the products accessible from CO₂ hydrogenation, providing another promising approach for HCHO synthesis in an energetically favorable and atom-efficient way.

2. Experimental procedures

2.1. Catalysts preparation

Ca-Al Layered double hydroxide (LDH) was prepared through a homogeneous alkalization reaction between an aqueous concentrated solution of CaCl₂·2H₂O and AlCl₃·6H₂O and propylene oxide. Certain amounts of CaCl₂·2H₂O and AlCl₃·6H₂O were dissolved in a mixture of ethanol and ultra-pure water. A certain amount of propylene oxide (PO, 99%, Macklin) was then added at 25 °C and further stirred for a few minutes to yield a homogeneous solution. The wet gels were then obtained through aging of the mixture for 24 h at 40 °C. After that, wet gels were submerged in 50 mL of isopropyl alcohol to exchange the liquid in the pores for three times. Finally, the wet gels were collected and dried at 40 °C for > 72 h. Ru/LDH was prepared through the impregnation of Ca-Al LDH with the dissolved RuCl₃·nH₂O (35.0–42.0% Ru basis, Aladdin) solution (0.4 g·L⁻¹). 0.4 g·L⁻¹ of the dissolved RuCl₃·nH₂O was diluted with water to obtain a total volume of 50 mL. Ca-Al LDH (0.5 g) was impregnated with RuCl₃·nH₂O solution and stirred at 50 °C for 12 h. During this step, Ru ions were introduced into the brucite layer of LDH due to “dissolution–precipitation” of LDH in water [34]. The resulting slurry was then recovered by filtration, followed by washing with the distilled water (Cl⁻ removal) and drying at 50 °C overnight, yielding Ru/LDH (Ru content: 0.1–3 wt%) as a gray powder. Ru/LDO-red was obtained by the reduction of Ru/LDH in 5% H₂/Ar mixture (50 mL·min⁻¹) at 500 °C for 1 h with a ramp rate of 10 °C·min⁻¹ from room temperature (r.t.) to 500 °C. Ru/LDO-oxi was obtained by the oxidation of Ru/LDH in air at 500 °C for 1 h with a ramp rate of 10 °C·min⁻¹ from r.t. to 500 °C. For comparison, the home-made SBA-15 (600 m²·g⁻¹) was used as the support to obtain Ru/SBA-15. The loading amount of Ru

varied in the range from 0.1%–3 wt%. Au/LDO-red, Rh/LDO-red, Pt/LDO-red, Ir/LDO-red, and Pd/LDO-red catalysts were also prepared via impregnation followed by reduction at 500 °C for 1 h under H₂ stream. The metal loading amount was 0.5 wt%, which was the same as Ru on Ru/LDO-red.

2.2. Catalysts characterization

The specific surface (BET) areas of the samples were measured using a surface area and porosity analyzer (ASAP2460, Micromeritics). X-ray diffraction (XRD) patterns were acquired using a x'pert3 powder (PANalytical B.V., Netherlands) with Cu K α radiation, operating at 40 kV and 40 mA. SEM images were obtained using a Nova NanoSEM 450 (FEI Company, Netherlands) system. Scanning transmission electron microscopy and energy-dispersive X-ray spectroscopy (STEM-EDX) were performed on a JEOL JEM-F200 and a JEOL JED-2300 T, respectively. X-ray photoelectron spectroscopy (XPS) were conducted with AXIS-ULTRA DLD-600 W (Shimadzu-Kratos Company, Japan). Ru K-edge X-ray absorption fine structure (XAFS) data were collected at BL14W beamline in Shanghai Synchrotron Radiation Facility (SSRF). The storage rings of SSRF were operated at 3.5 GeV with a stable current of 200 mA. Using Si (111) double-crystal monochromator and Lytle detector, experiments were carried out in transmission mode under ambient conditions. XAFS data were examined using the Athena program.

2.3. Catalytic activity measurement

Catalytic activity measurements were performed in the batch reactor or flow reactor system. The details were shown in Fig. S10. In a typical experiment for the batch reactor, the catalyst (50 mg) and deionized water (10 mL) were loaded into an autoclave. After replacing air with CO₂, 10 bar of CO₂ was charged into the reactor and then the pressure was increased to 20 bar with 10 bar of H₂. The temperature of the system was kept at 30 °C and stirred at 300 rpm for 12 h. As for experiments in the flow reactor, the Ru/LDH-red catalyst was dispersed in 50 mL of H₂O in a round-bottomed flask under stirring, as shown in Fig. S10. The reactor containing the suspension was firstly degassed with CO₂ (20 mL·min⁻¹). The catalytic testing was then carried out at ambient pressure with a flow of CO₂ (5 mL·min⁻¹) and H₂ (5 mL·min⁻¹). After reaction, liquid samples were collected through centrifugation and filtration for further analysis. The product yields in liquid were determined by HPLC using an Agilent 1260 HPLC instrument (Agilent Technologies Company, America) equipped with an Aminex HPX-87 H Ion Exclusion Column and 5 mM H₂SO₄ (0.500 mL·min⁻¹) as the mobile phase at 35 °C.

To confirm the production of HCHO derived from CO₂ gas, we carried out ¹³C isotope experiment in the batch reactor. Specifically, the catalyst (50 mg) and deuterium oxide (10 mL D₂O) were loaded into an autoclave. Then 1 bar of ¹³CO₂ (¹³CO₂ with 99% ¹³C atom, Niuruide gas company in China) and 1 bar of H₂ were fed into this reaction system. The temperature of the system was kept at 30 °C and stirred for 12 h. Liquid products were analyzed using an AVIII 400 MHz NMR spectrometer (Bruker AscendTM 600 MHz, Swiss Confederation). A water suppression method was used for ¹H NMR analysis. ¹³C NMR was used for carbon analysis.

In order to study the reaction intermediate, CO hydrogenation was carried out in the batch reactor mentioned above. In the experiment for CO hydrogenation, 1 bar of 10%CO/Ar mixture and 1 bar of H₂ were charged into the reactor. Hydrogenation of formic acid was performed via dissolving formic acid in water in the batch reactor and loading H₂ gas. liquid samples were collected after reactions and determined by HPLC.

2.4. In-situ DRIFTS study

DRIFTS experiments were conducted using a reaction chamber (HTC,

Harrick Scientific Products Inc., USA) coupled with a Fourier transform infrared (FTIR) spectrometer (Nicolet IS50, Thermo Fisher, USA). A mercury cadmium telluride (MCT) detector was used and cooled with liquid nitrogen. The flow rates of reactant gases were controlled by mass flow controllers (Sevenstar D07-19B/ZM, Beijing Sevenstar Electronics Ltd., China). The OMNIC software (Thermo Scientific) was used to collect spectrometer data at specific time intervals. Prior to the tests, the loaded sample in the chamber was soaked with a few drops of ultra-pure water and slightly pressed to obtain a flat and even surface. CO₂ flow was then introduced into HTC with 40 mL min⁻¹ of flow rate for 60 mins at 30 °C and then shifted to N₂ purge. When N₂ was shut down, background data started collection. CO₂ was then introduced to the sample and the transient DRIFTS IR spectra was recorded via six scans at a resolution of 4 cm⁻¹ in each 10 s. H₂ was subsequently introduced, followed by CO₂ closing and H₂ shutting down. During the procedure, IR spectra were recorded.

2.5. DFT calculation

All first-principles spin-polarized calculations were performed using the Vienna ab initio simulation package. Ion-electron interactions were described by the projector augmented wave method, and the generalized gradient approximation in the Perdew–Burke–Ernzerhof form and a cutoff energy of 400 eV for plane-wave basis set were adopted. The convergence threshold was 10⁻⁵ eV, and 5 × 10⁻³ eV/Å for energy and force, respectively, during the structure relaxation. The weak interaction was described by DFT+D3 method using empirical correction in Grimme's scheme. The vacuum space was set to be more than 12 Å, which was enough to avoid the interaction between periodical images. For Ru/LDH and Ru/LDH-red catalysts, two layers of Ca-Al LDH with one CO₃²⁻ layer between the LDH layers was built during the optimization, and the Ca/Al ratio was set to be 3/1. The location of Ru on LDH was simulated based on catalyst configuration reflected by XRD, TEM and XAFS analysis. Furthermore, the implicit solvent effect has also been considered during the calculation model with water as implemented in VASPsol to mimic real experimental conditions. The minimum energy pathway was determined using a climbing image nudged elastic band method (CINEB). The reaction Gibbs free energy changes (ΔG) for each elementary step can be calculated by the following equation: ΔG = ΔE + ΔZPE - TΔS, where ΔE is DFT calculated energy difference between reactants and products, ΔZPE is the change of zero-point energies (ZPE), T is the temperature of 298.15 K, and ΔS is the change in entropy of products and reactants.

3. Results and discussion

3.1. Synthesis of LDH-supported Ru catalysts

Layered double hydroxides (LDH), with a general formula of [M₁²⁺_{1-x}M₂³⁺_x(OH)₂]^{z+} A_{z/n}ⁿ⁻•mH₂O, in which M²⁺ and M³⁺ occupy the octahedral holes in a brucite-like layer and Aⁿ⁻ represents the exchangeable interlayer anions to compensate the positive charge on the layers, has been widely employed in CO₂-related research terms [35–38]. As the catalyst support or catalyst, LDH offers: (i) six-fold coordinated OH- groups with cations that can facilitate chemisorption and activation of CO₂; (ii) coordinatively unsaturated active sites to promote metal dispersion. Moreover, Ru has received great attention among precious metals for activating CO₂. Various supports (e.g., TiO₂, CeO₂) supported Ru have been reported for the hydrogenation of CO₂ to CO [39] and CH₄ [40,41] in the gas phase or HCOOH [42,43] and CH₃OH [44] in the liquid phase. These studies pointed out the plausible reaction pathways involving CO₂ adsorption on H-terminated Ru surfaces, and the further hydrogenation steps using chemisorbed *H to *C_xH_yO intermediate species. Therefore, LDH-supported Ru catalysts were designed and prepared in the present study, as shown in Fig. 1.

Ca-Al LDH materials were obtained through a homogeneous alkalization reaction between an aqueous concentrated solution of metal salts and propylene oxide (PO). The incorporation of PO can induce a modest elevation of pH. The following phase separation parallel with sol-gel transition improves the formation of mm-sized channel (macrochannel). The nm-sized channel (mesochannel) spontaneously forms as interstices between co-continuous phase-separated domains solidified by the sol-gel reaction. Such special nano structure (e.g. Ni-Al LDH nanocrystals, ~20 nm) presents high affinity towards gaseous CO₂ [45]. Thermal treatment of LDH supported catalysts such as Ru/LDH in air or H₂/Ar mixture at high temperature (500 °C) can completely remove interlayer water molecules, anions and surface hydroxyl groups of LDH, leaving the corresponding metal oxides (LDO) behind [46–48]. These mixed metal oxides can be regenerated back to LDH when they are immersed in water. Herein, the thermally-treated catalysts immersed in water to perform hydrogenation of CO₂ will transferred into LDH-supported Ru catalysts. And such transferred catalysts are the actual catalysts during the reaction, which were thus denoted as Ru/LDH-red or Ru/LDH-oxi.

3.2. Characterization of LDH-supported Ru catalysts

The Ca-Al LDH were mostly composed of thin plates, possessing a regular hexagonal structure with an approximate size around 5 μm (Fig. S1). Being different from the smooth surface of pure Ca-Al LDH, the

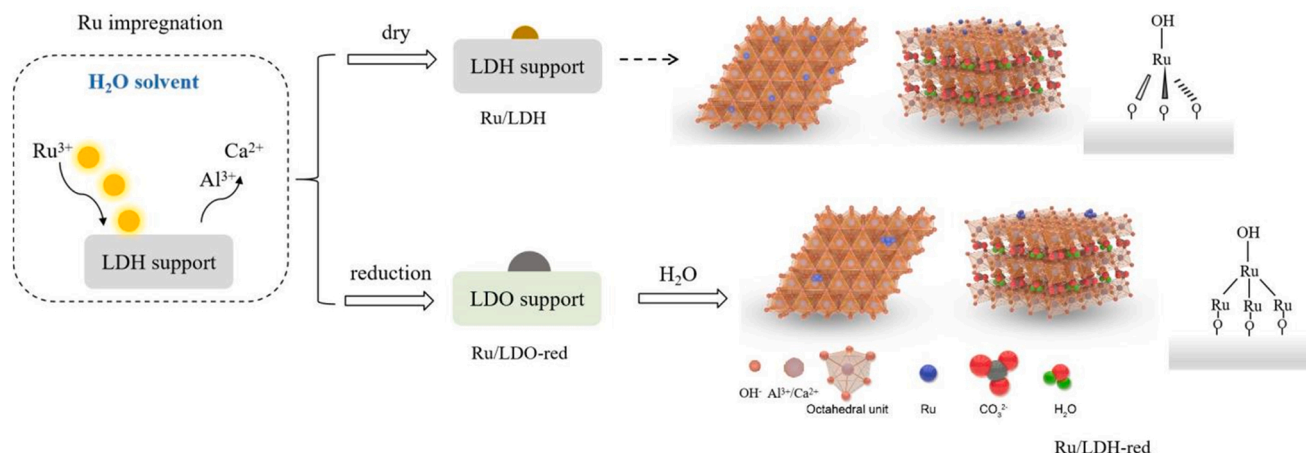


Fig. 1. Schematics of the fabrication process of the catalysts.

surface of Ru/LDH was rough and covered with fine flakes (Fig. 2(A)). The absorption-desorption isotherm of Ru/LDH exhibited properties of microporous adsorbents [49,50], with the specific surface area of $25.6 \text{ m}^2 \cdot \text{g}^{-1}$ and total pore volume of $0.08 \text{ cm}^3 \cdot \text{g}^{-1}$ (Fig. S2). The pores of Ru/LDH are mostly distributed over a range of 2–10 nm. Ru/LDH-red also possesses hexagonal structure of Ca-Al LDH, however, its structure is irregular and surface is much rough, as shown in Fig. 2(B). The crystallinity of a Ca-Al LDH is assessed by XRD measurements. The characteristic peaks of $\text{Ca}_{0.8}\text{Al}_{0.2}(\text{OH})_2\text{Cl}_{0.2}$ were shown in the XRD pattern of Ca-Al LDH (Fig. 2(C)) [51,52]. The XRD pattern of Ru/LDH shown in Fig. 2(C) only exhibits the characteristic peaks of $\text{Ca}_{0.8}\text{Al}_{0.2}(\text{OH})_2\text{Cl}_{0.2}$ and does not contain any crystal phases of Ru (such as Ru or RuO_2). The XRD pattern of Ru/LDH-red exhibited characteristic peaks of Ca-Al LDH with a much lower intensity than Ru/LDH (Fig. 2(C)). Impressively, we observed some Ru nanoparticles with an average particle size of 2.4 nm (Fig. S5) and clear lattice spacings of Ru [101] in TEM images of the Ru/LDH-red (Fig. 2(B)). HAADF-STEM and elemental mapping images shown in Fig. S4 and Table S3 further demonstrated Ru aggregation on Ru/LDH-red clearly. It means that reduction under thermal conditions induced Ru species' agglomeration. In contrast, Ru species in Ru/LDH were highly dispersed over LDH, Ru signal was not detected from its elemental mapping images (Fig. S3 and Table S2).

In order to dig deeper out the properties of Ru for both Ru/LDH and Ru/LDH-red, both XPS and XAFS techniques were used. The weak Ru 3p spectrum peak located at 461.5 eV could be observed on Ru/LDH (Fig. S6). As for Ru/LDH-red, the Ru 3p spectrum peak was located around 459.0 eV, which shifted toward lower binding energy than the peak on Ru/LDH. Such shift indicated more metallic Ru present over Ru/LDH-red than Ru/LDH. The electronic state and coordination environment of Ru/LDH and Ru/LDH-red can be further elucidated by ex-situ Ru K-edge XANES/EXAFS results (Fig. 2(E-F)). Compared to reference Ru foil, RuCl_3 and RuO_2 , the Ru K-edge XANES (Fig. 2(E)) verified that the oxidation state of Ru for Ru/LDH is +4 according to its position of the absorption edge. EXAFS spectrum of Ru/LDH shown in Fig. 2(E) presents Ru-O bonds, which indicating the strong interaction between Ru and the support Ca-Al LDH. The white line feature of Ru/LDH-red indicates that the Ru species may adopt a hybrid property. Its EXAFS spectra shown in Fig. 2(E-F) further clarify both Ru-O and Ru-Ru bonds present for the Ru/LDH-red catalyst. The Fourier-transformed R-space EXAFS spectra (Figs. S7–S9) together with the fitting results (Table S5–7) show the presence of Ru-O first shell (bond distance $\approx 1.99 \text{ \AA}$, coordination number (C.N.) ≈ 2.1), Ru-O second shell (bond distance $\approx 2.04 \text{ \AA}$, coordination number (C.N.) ≈ 1.1) and Ru-Ru shell (bond distance $\approx 2.67 \text{ \AA}$, coordination number (C.N.) ≈ 4.1) in the Ru/LDH-red catalyst (Fig. 2(F)). The absence of Ru-Ru shell over Ru/LDH is consistent with our TEM/SEM observation. Those results indicated that Ru in Ru/LDH is in the form of small RuO_2 clusters without long-range order.

3.3. CO_2 hydrogenation over the catalysts

A typical reaction of CO_2 hydrogenation was performed in a stainless-steel autoclave reactor with 10 mL of water and 50 mg of the catalyst in the absence of additives under 10 bar CO_2 and 10 bar H_2 at 30°C for 12 h (Fig. S10). Fig. 3 (A) shows the conversions of gaseous CO_2 after 12 h reactions over the different catalysts. The Ru/LDH-red exhibited much higher CO_2 gas conversion than LDH supported other metal catalysts, such as Pt, Pd, Ir, Rh, Au, and LDH itself. In the cases of Ru/LDH-red and Pt/LDH-red, the pressure of the batch reactor after the reactions decreased to about 1 atm, the conversions of gaseous CO_2 reaching about 90%. At 30°C , the solubility of 10 bar CO_2 in water is rather low, generally less than 1 mol/kg [53]. Therefore, the pressure decrease of the autoclave strongly indicated that the loaded gaseous CO_2 was converted into other species. With the analysis of solution after reactions by high performance liquid chromatography (HPLC), both HCHO and formic acid (HCOOH) were detected when Pd/LDH-red was used as the catalyst. In the case of Ru/LDH-red with 0.5 wt% of Ru,

HCHO was detected as the only product in liquid, as shown by the HPLC spectra of the solutions in Fig. S11 and our previous report [54]. The formation of HCHO in aqueous media was also confirmed with the colorimetric 3-methyl-2-benzothiazolinone hydrazone (MBTH) method [55]. The typical blue-green color can be observed (Figs. 3(D) and S12), which strongly suggests the presence of HCHO in the solution. It was also worthy to note that HCHO can react with water rapidly to form methylene glycol ($\text{CH}_2(\text{OH})_2$) [56]. HCHO and $\text{CH}_2(\text{OH})_2$ co-exist in a dynamic equilibrium with a $\text{HCHO}/\text{CH}_2(\text{OH})_2$ ratio of 1:2499 at STP and $\text{pH} = 7$, which means that 99.96% of HCHO is converted to $\text{CH}_2(\text{OH})_2$. $\text{CH}_2(\text{OH})_2$ can further polymerize to form polyoxymethylene ($(\text{CH}_2\text{O})_n$), e.g. sym-trioxane ($\text{C}_3\text{H}_6\text{O}_3$) [57,58]. Therefore, produced HCHO seems instantly absorbed in water, thus further improves CO_2 hydrogenation.

The catalytic hydrogenation activities of CO_2 to HCHO over various Ru-based catalysts were compared with the yield of formaldehyde ($\text{mmol} \cdot \text{L}^{-1} \cdot \text{gcat}^{-1}$) and turnover number (TON) based on Ru. The geometric and electronic properties of Ru were firstly tuned via thermal treatments of Ru/LDH in oxidative or reduction atmospheres. As shown in Fig. 3 (B), the state of Ru on LDH likely plays a key role in the reaction. The catalytic activity of Ru/LDH was drastically enhanced via the reduction. The average molar yield of HCHO over Ru/LDH-red catalysts was $583 \text{ mmol} \cdot \text{L}^{-1} \cdot \text{gcat}^{-1}$, much higher than that over Ru/LDH and Ru/LDH-oxi. The molar yields of HCHO over Ru/LDH and Ru/LDH-oxi were 297 and $222 \text{ mmol} \cdot \text{L}^{-1} \cdot \text{gcat}^{-1}$, respectively. Furthermore, a heterogeneous Ru/SBA-15 did not show efficient catalysis, suggesting the importance of support LDH in CO_2 hydrogenation. Both Ru clusters with special electronic states and CaAl-LDH with abundant hydroxyl groups are indispensable in achieving high catalytic activity. Fig. 3 (C) shows effects of Ru loading amount of Ru/LDH and Ru/LDH-red on HCHO and HCOOH yields. The average molar yields of HCHO for Ru/LDH catalysts with 0.1 wt% Ru and 0.5 wt% Ru were 280 and $297 \text{ mmol} \cdot \text{L}^{-1} \cdot \text{gcat}^{-1}$, respectively. Increasing Ru loading amount to 1 wt% or 2 wt% did not improve the yield of HCHO. The average molar yield of HCHO for Ru/LDH catalysts with 3 wt% Ru was $319 \text{ mmol} \cdot \text{L}^{-1} \cdot \text{gcat}^{-1}$. This result indicated that the production rate of HCHO was not proportional to the amount of Ru in the case of Ru/LDH. More interestingly, HCOOH was detected when Ru/LDH-red with high Ru loading amount was used as the catalyst. It was shown in Fig. 3 (C) that the yield of HCHO decreased, while the yield of HCOOH increased with the increase of Ru loading amount for Ru/LDH-red catalysts. The amount of Ru for Ru/LDH-red catalyst affect the products' distribution and their amounts.

Since Ru/LDH-red with 0.5 wt% of Ru provided the highest activity in the batch reactor system, this catalyst was then used in the flow reactor system at the ambient pressures of CO_2 and H_2 (the total flow rate is $10 \text{ mL} \cdot \text{min}^{-1}$, $\text{CO}_2/\text{H}_2 = 1:1$). Fig. 3(D) shows the molar yields of HCHO with time in a flow reactor system under ambient conditions at 18°C . This result demonstrates the high catalytic activity and selectivity of Ru/LDH-red in the hydrogenation of CO_2 . Moreover, the production rate of HCHO also increased with increasing pressure of H_2 and CO_2 (Fig. 3(E)). The HCHO yield of $749 \text{ mmol} \cdot \text{L}^{-1} \cdot \text{gcat}^{-1}$ were achieved over Ru/LDH at 30°C with 20 bar of CO_2 and 20 bar of H_2 . With varying H_2 or CO_2 partial pressure, it was found that the H_2 to CO_2 ratio of 1 can afford highest HCHO yield over the Ru/LDH-red catalyst (Fig. S13). Furthermore, the 0.5 wt% Ru/LDH-red heterogeneous catalyst can be repeated used. There is still the activity for HCHO formation after 6 times, as shown in catalyst recyclability tests in Fig. S14. Fig. 3 also indicated that low reaction temperature is more conducive to a higher yield of HCHO, where 30°C affords the highest HCHO yield with 0.5 wt % Ru/LDH-red. It is consistent with the exothermic nature of CO_2 hydrogenation with H_2 in water and the decreased aqueous solubilities of both CO_2 and H_2 under higher temperatures.

3.4. Mechanistic investigations

HCHO was clearly detected in reaction solution, but the reaction pathway of CO_2 hydrogenation into HCHO ($\text{CO}_2 \text{ aq} + 2 \text{ H}_2 \text{ aq} \rightarrow \text{HCHO}$

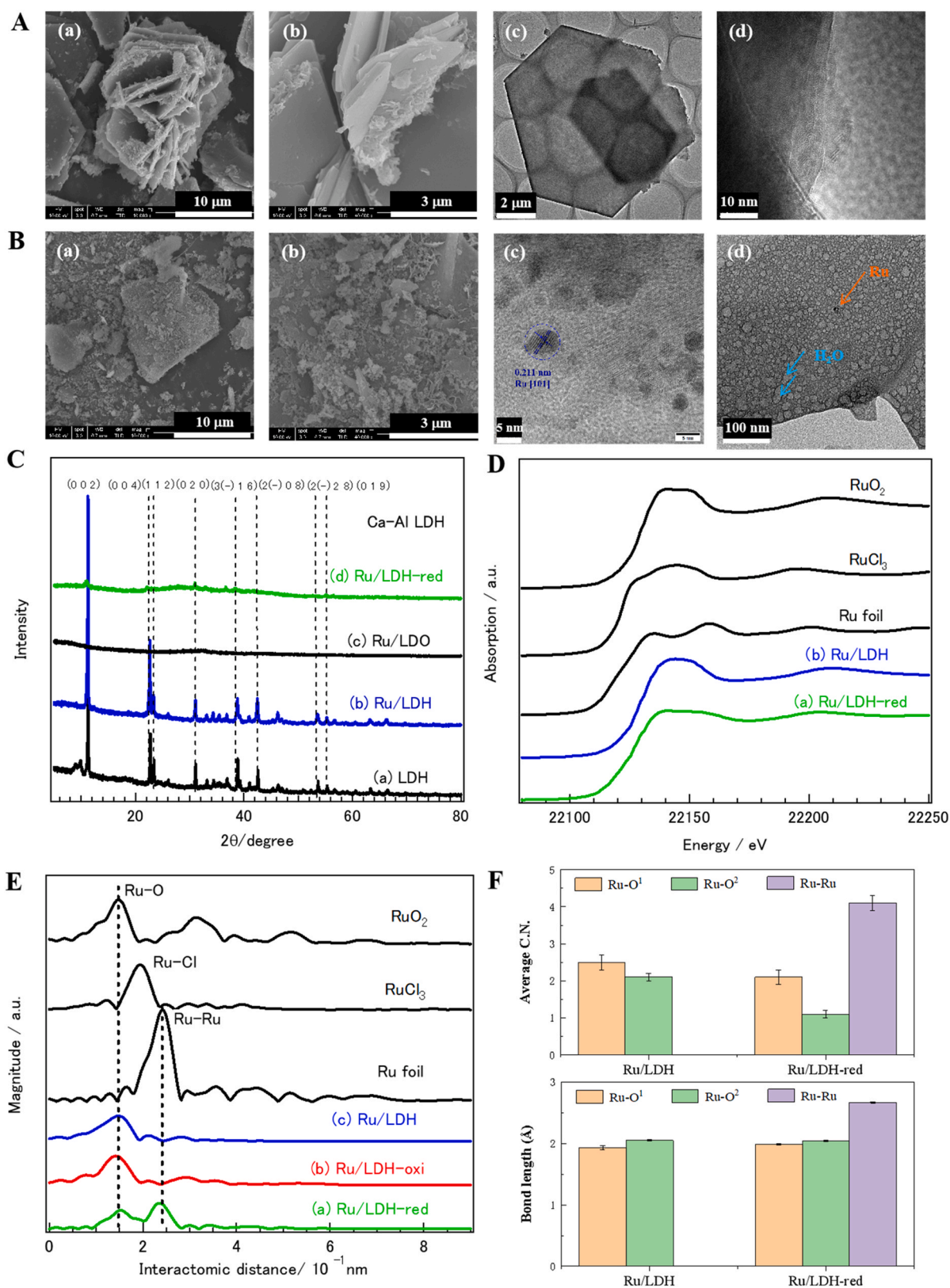


Fig. 2. Catalyst characterization. (A and B) Representative SEM (a-b) and TEM images (c-d) of Ru/LDH (A) and Ru/LDH-red (B) catalysts. (C) XRD patterns of LDH, Ru/LDH and Ru/LDH-red. (D) Ru K-edge XANES spectra of Ru/LDH-red and Ru/LDH. Ru foil, RuCl₃, RuO₂ and Ru/LDH-oxi were used as references. (E) The k^3 -weighted Fourier transform EXAFS spectra of Ru/LDH and Ru/LDH-red. (F) Evolution of the average coordination number (C.N., normalized to all Ru atoms) and bond length with the corresponding conditions described in Fig. 1 (E). “Ru–O” refer to the ruthenium–oxygen bond of the Ru/LDH-red and Ru/LDH interfaces. “Ru–O¹” and “Ru–O²” represent the shorter and longer metallic bonds around the Ru absorber, respectively. Note: Ru loading amounts over the Ru/LDH, Ru/LDO, Ru/LDH-oxi and Ru/LDH-red mentioned in figure are same, being 0.5 wt%.

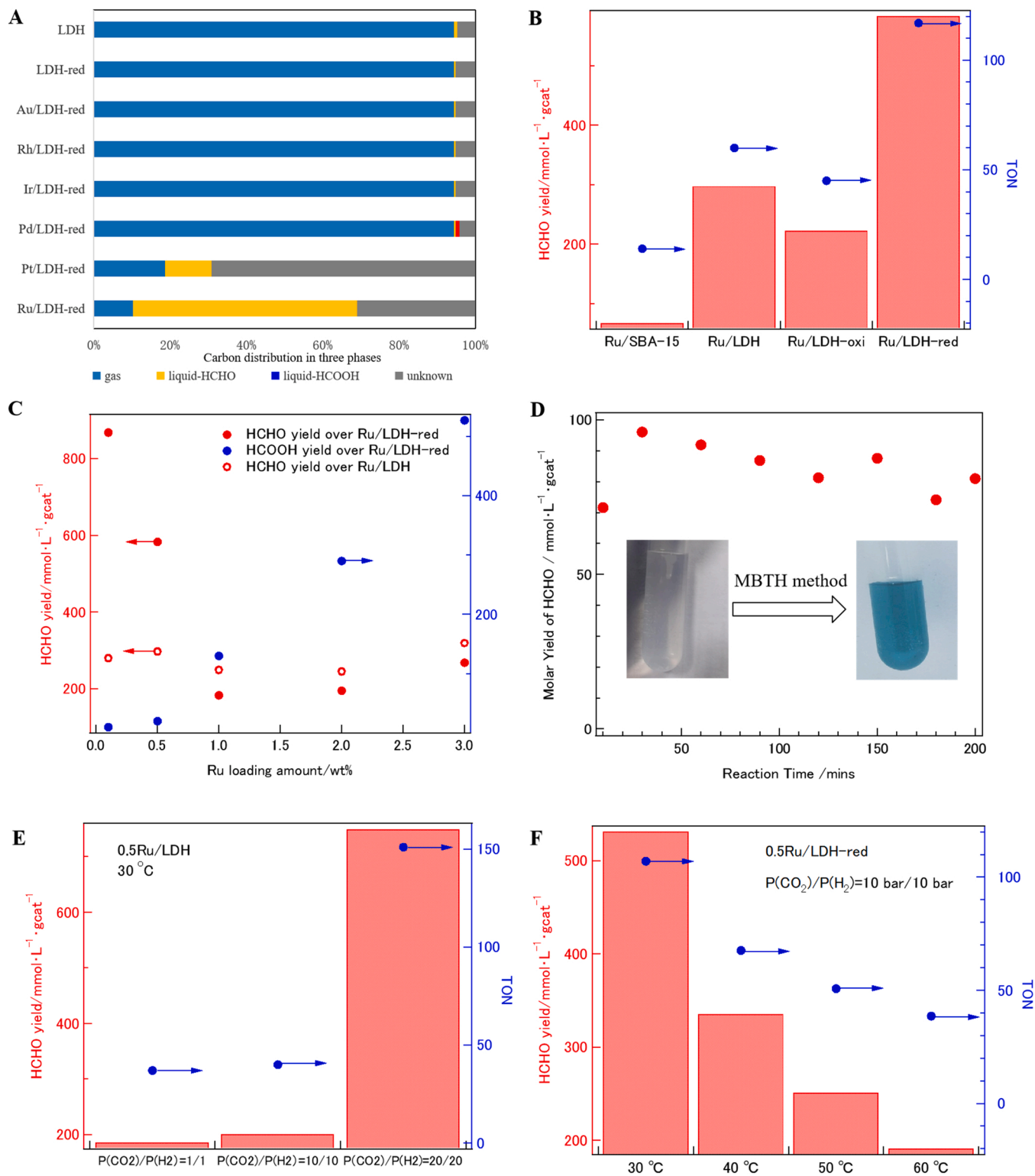


Fig. 3. Catalytic performance in CO_2 hydrogenation. (A) Comparison of carbon-distribution after 12 h of reaction over the Ru/LDH-red and other catalysts in a batch reactor under the reaction conditions: 10 mL of water, 10 bar CO_2 and 10 bar H_2 , 30 $^{\circ}\text{C}$, 50 mg catalyst. (B) HCHO yields and TON values in CO_2 hydrogenation over different catalysts in a batch reactor under the reaction conditions: 10 mL of water, 10 bar CO_2 and 10 bar H_2 , 30 $^{\circ}\text{C}$, 50 mg catalyst with 0.5 wt% Ru. (C) Effects of Ru loading amount of Ru/LDH and Ru/LDH-red on HCHO and HCOOH yields under the reaction conditions: 10 mL of water, 10 bar CO_2 and 10 bar H_2 , 30 $^{\circ}\text{C}$, 50 mg catalyst. (D) Catalytic performances of 0.5 wt% Ru/LDH-red catalyst for CO_2 hydrogenation in a flow reactor (reaction conditions: 5 $\text{mL} \cdot \text{min}^{-1}$ CO_2 , 5 $\text{mL} \cdot \text{min}^{-1}$ H_2 , 18 $^{\circ}\text{C}$, 50 mg catalyst, 50 mL H_2O). The inset is the reaction solutions before and after adding MBTH, HCl and ammonium ferric sulfate at 313 K for 10 mins. (E) Effects of CO_2 and H_2 pressures on HCHO yield (reaction conditions: 10 mL of water, 30 $^{\circ}\text{C}$, 50 mg 0.5 wt% Ru/LDH). (F) Effects of reaction temperature on HCHO yield (10 mL of water, 10 bar CO_2 and 10 bar H_2 , 30 $^{\circ}\text{C}$, 50 mg 0.5 wt% Ru/LDH-red).

aq + H₂O) in water is unclear. As is well known, CO₂ dissolved in water is in equilibrium with two other forms: HCO₃⁻ and CO₃²⁻, and their mole fraction distribution changes with the pH level in water (Fig. S17). In our experiments, ultra-pure water was used as the reaction solution without additives. Thus, both dissolved CO₂ (CO₂ aq) and HCO₃⁻ were supposed to exist in the water. The reactivity of H₂ with CO or HCOOH over 0.5Ru/LDH-red was explored further to understand the intermediates and reaction route. As shown in Fig. 4(A), on the charge of 1 atm of CO and H₂ to the reactor in the presence of the active catalyst, HCOOH formation was observed. HCHO can hardly be seen in the reaction solution. Based on the HPLC spectra, HCOOH species was identified as the only product of CO hydrogenation. Fig. 4(B) depicted the HPLC spectra of the solution after the reactivity of H₂ with HCOOH dissolved in water. A peak that corresponded to HCHO species was observed at 6.8 mins besides one strong peak assigned to HCOOH substrate at 16.0 min. A comparison of Fig. 4(A) and (B) indicated that HCOOH, not CO, is one important reaction intermediate for CO₂ hydrogenation to HCHO.

More details on the variation trend of CO₂ over the catalysts have been systematically investigated by vibrational spectroscopy. Since the fine structure of the heterogeneous catalysts drastically influences the formation of intermediates and products [59–61], DRIFTS on Ru/LDH and Ru/LDH-red catalysts were measured in the present work. Fig. 4 (C–D) show the DRIFTS spectra of CO₂ hydrogenation under different transient conditions over soaked Ru/LDH and Ru/LDH-red catalysts, respectively. The IR features developed with CO₂ exposure are related to adsorbed species on the catalyst, and gas-phase CO₂ (2351, 2325, 2275 cm⁻¹ for Ru/LDH and 2360, 2337, 2268 cm⁻¹ for Ru/LDH-red). No adsorbed CO species were observed. The presence of multiple peaks in the region of 3750–3500 cm⁻¹ can be attributed to both CO₂ overtones (~3700 and 3600 cm⁻¹) and adsorbed bicarbonates (~3740 and 3640 cm⁻¹) [62–65]. In comparison, the peak intensities of CO₂ and HCO₃⁻ on Ru/LDH-red were obviously higher than those on Ru/LDH. With the introduction of H₂, the peak intensities of CO₂ and HCO₃⁻ became weaker, especially over Ru/LDH-red. The evolution of the peaks in the region of 1480–1660 cm⁻¹ (for Ru/LDH) and 1430–1630 cm⁻¹ (for Ru/LDH-red), which are attributed to the C–H stretching mode and the O–C–O bending mode combinations (Table S8) [66,67], indicated the formation of formate species. These phenomena can be still observed when the CO₂ gas feeding was closed. The IR signals due to CO₂ and HCO₃⁻ continuously disappeared, while those of formate species became more obvious. It was more worthy to note that HCHO signal was detected at 1793 cm⁻¹ over Ru/LDH-red, in well agreement with the catalytic tests. Concurrent with the HCHO formation, a negative peak around 3700 cm⁻¹ appeared, which was assigned to the consumption of -OH groups on LDH surface [68]. Based on these experimental measurements, we hypothesized the possible reaction route involving formic acid as an intermediate (CO₂ aq + H₂ aq → HCOOH aq; HCOOH aq + H₂ aq → HCHO aq + H₂O l).

The experimental observations motivated DFT calculations to bring fundamental theoretical insights into the reaction mechanism. The catalyst systems, Ru/LDH and Ru/LDH-red were simulated, as shown in Fig. 5(A), to shed light on the relationship between catalyst surface and the adsorption of CO₂ and H₂. The electronic states of Ru in Ru/LDH-red were predicted based on theoretical calculation of the catalyst. Charge density difference shown in Fig. 5(A) illustrates a perturbation of the electron density near the Ru atoms and the atomic hybrid of both Ru⁰ and Ru⁴⁺ in Ru/LDH-red. The bottom three Ru atoms surrounded by the hydroxyl groups, transfer charges to the LDH. However, there is no clear charge transfer for the top single Ru atom. Its electronegativity was enhanced by such special location of Ru atoms and hydroxyl groups on LDH. We also followed previous researchers' methods [69] and added water molecules in our model to simulate water environment. Most suitable configuration of species and intermediates during CO₂ hydrogenation over Ru/LDH or Ru/LDH-red during DFT calculations were shown in Figs. S18 and S19. The Gibbs free energy change diagrams for CO₂ reduction calculated using DFT have been shown in Fig. 5(B).

The CO₂ adsorption step is found to be a spontaneous process with the negative free energy change, and is more favorable over Ru/LDH-red than Ru/LDH. Gong et al. once reported that surface -OH was beneficial to CO₂ adsorption in the form of H₂CO₃ via hydrogen bonds [69]. In the present work, LDH surface is rich of hydroxyls, thus it is rational to suppose that CO₂ molecules are adsorbed on the -OH of Ru/LDH-red surface, followed by a rapid balance between CO₂ and H₂CO₃ in water. With the introduction of H₂, the dissociative adsorption of H₂ occurred. The preferred dissociative adsorption of H₂ on Ru was previously reported [70,71]. The calculated energy barrier for H₂ dissociation on Ru/LDH-red here is 0.51 eV, less than that for Ru/LDH catalyst (0.66 eV). It was indicated that H₂ dissociation is more favorable on the former one. Then the adsorbed *CO₂ can attack one proton-electron pair to form *HCOOH species. As illustrated in Fig. 5(B) and (D), the formation of *HCOOH species is also favorable on Ru/LDH-red compared to Ru/LDH. Next, the dissociative adsorption of H₂ continue on Ru cluster, which induced the formation of *HCO intermediate and release of one water molecule. The calculated energy barriers are 0.96 eV and 1.20 eV for Ru/LDH-red and Ru/LDH, respectively. The adsorbed *HCO species continue reacting with another *H until HCHO formed on the catalyst surface, and all the required energies input for these two processes are lower than 0.45 eV. The step from *HCOOH species towards *HCO on the catalyst surface is the rate limiting step (RLS) during the whole CO₂ reduction process. To further verify that HCHO was produced from the hydrogenation of gaseous CO₂, the experiment was also reproduced with an isotopically labeled ¹³CO₂. The ¹³C NMR and ¹H NMR splitting patterns of the labeled carbons in HCHO and HCOOH, shown in Fig. 5(C) supports that these products were derived solely from the labeled CO₂ gas. On the basis of these results, it can be established that CO₂ gas can be reduced by H₂ to HCHO in water in the presence of the catalyst, and HCOOH is the important reaction intermediate.

In summary, the DFT calculations suggest that the formation of HCHO is easily proceeding on the Ru/LDH-red catalyst via HCOOH pathway (Fig. 5(D)). It is reported that the strong electron-donating ability of PNP pincer-type ligands or N-heterocyclic carbenes in Ir(III) complexes (homogeneous catalyst) facilitates hydrogenation of CO₂ [72]. Moreover, there is a linear correlation between the hydrogenation rate and the electron-donating ability of bipyridine ligands with various substituents [73]. Taking these results as reference, one important reason for the high catalytic activity of Ru/LDH-red is ascribed to an electron-rich Ru. This hybrid electronic state of Ru and a deep affinity with CO₂ of LDH in the Ru/LDH-red catalyst contribute to overcoming the energy barrier for the formation of *HCO species accompanied with H₂ dissociation, affording its superior catalytic performances even at ambient conditions.

4. Conclusions

We present a more environmentally friendly and efficient route to produce HCHO beyond the energy-intensive formox process. Ru/LDH-red catalyst, due to the hybrid electronic state of Ru nanoparticles and rich surface -OH of LDH, as well as their synergistic effect, can highly efficiently catalyze heterogeneous hydrogenation of CO₂ to formaldehyde in liquid water at near ambient temperature and pressure. The highest molar yield of HCHO of 583 mmol·L⁻¹·gcat⁻¹ in water at 30 °C with 10 bar CO₂ and 10 bar H₂ was achieved. The reaction mechanism involving *HCOOH was proposed based on experimental findings together with DFT calculations. The findings widen the value-added products from CO₂ hydrogenation besides CO, methanol and methane, also demonstrate a deeper mechanistic study to understand the reaction process.

CRedit authorship contribution statement

M. Xu, X. Liu and L. Deng acquire funding. X. Liu and L. Deng conceived and designed the project. L. Deng carried out sample

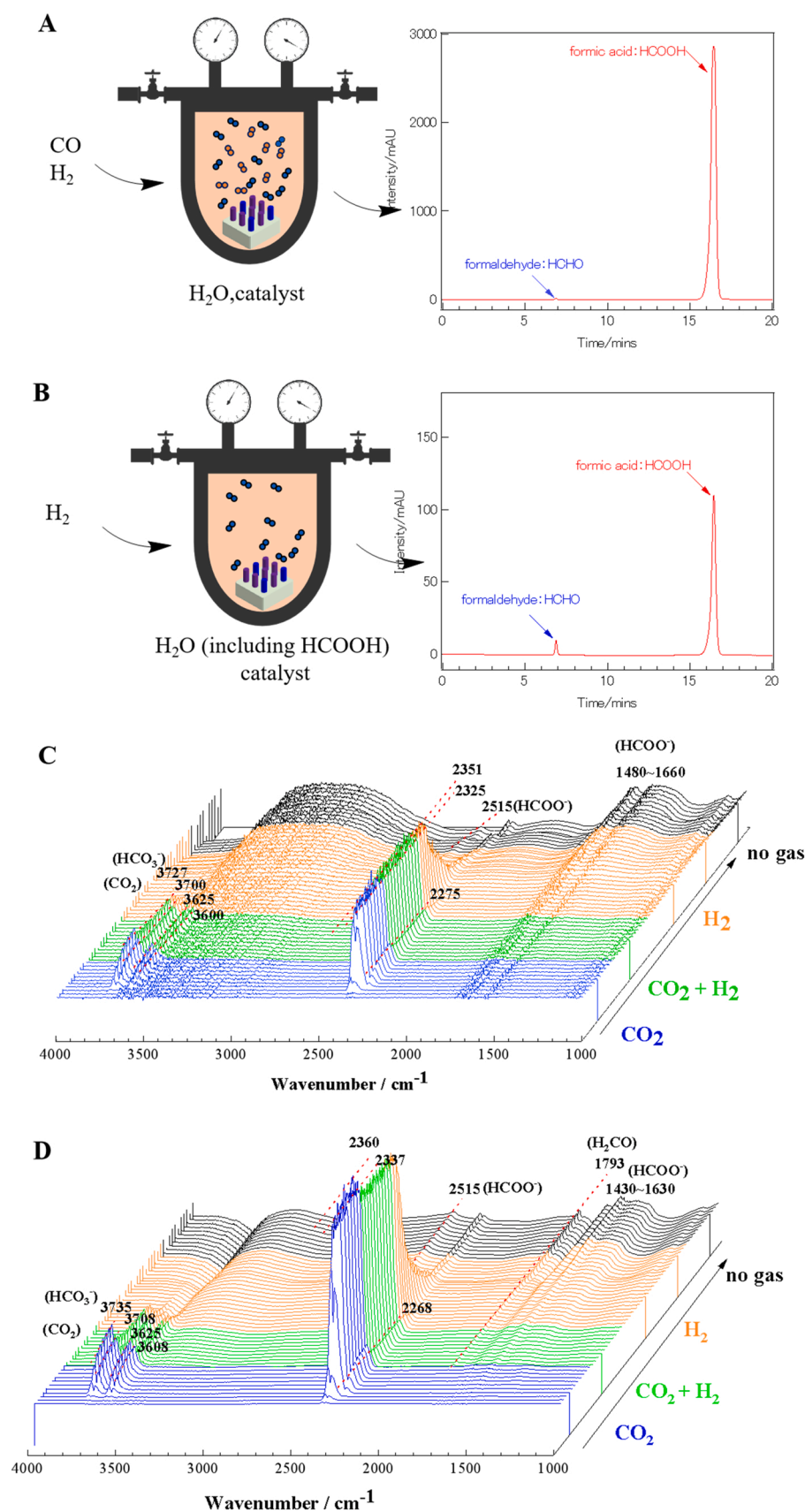


Fig. 4. Reaction Intermediate Species. (A) HPLC spectra of the aqueous products of CO reduction with H₂ over 0.5 wt%Ru/LDH-red. (B) HPLC spectra of the aqueous products of formic acid reduction with H₂ over 0.5 wt%Ru/LDH-red. (C and D) In-situ DRIFTs spectra from CO₂ hydrogenation over 0.5 wt%Ru/LDH (C) and 0.5 wt%Ru/LDH-red (D). The data were collected at 30 °C over the catalyst with the introduction of CO₂, H₂ gas followed by their shutting down, during which both flow rates of H₂ and CO₂ were 40 mL min⁻¹. The catalyst was first soaked with a few drops of ultra-pure water and then pre-adsorbed CO₂ with 40 mL min⁻¹ of CO₂ flow rate, followed by N₂ purge.

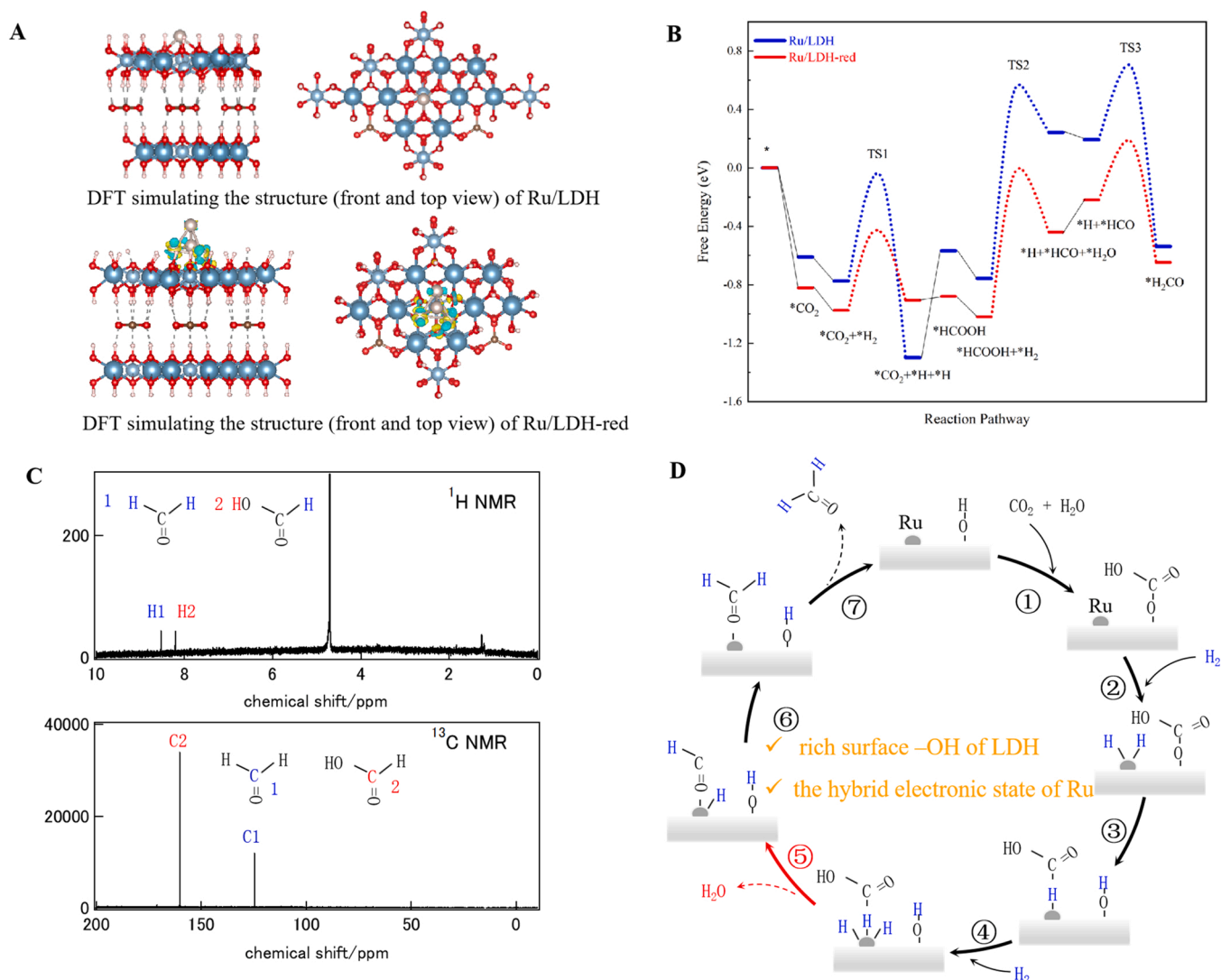


Fig. 5. Catalytic reaction route. (A) DFT simulations indicating the structure (front and top view) of 0.5 wt%Ru/LDH and 0.5 wt%Ru/LDH-red. Charge density difference of Ru atoms over Ru/LDH-red. Yellow area indicates the charge accumulation, while cyan area indicates the charge depletion. The red, silver, gray, big blue and small blue balls refer to O, Ru, C, Ca, and Al atoms, respectively. (B) Calculated Gibbs free energy change diagram for CO₂ reduction to HCHO on 0.5 wt% Ru/LDH-red and 0.5 wt%Ru/LDH through the HCOOH pathway. (C) ¹H NMR and ¹³C NMR spectra of the aqueous products of ¹³CO₂ reduction on 0.5 wt%Ru/LDH-red. (D) Proposed catalytic cycle for CO₂ hydrogenation over 0.5 wt%Ru/LDH-red.

preparation, and XRD, SEM, TEM, XPS, XAFS data analysis, as well as CO₂ hydrogenation reactions. Deng, X. Li and Z. You performed the operando DRIFT spectroscopic experiments and the corresponding data analysis. L. Deng performed the DFT calculation, and prepared the first version of the manuscript. Z. Wang, X. Jiang, M. Ding contributed to valuable discussion. All authors discussed the results and commented on the manuscript.

Declaration of Competing Interest

The authors declare that they have no known competing financial interests or personal relationships that could have appeared to influence the work reported in this paper.

Data availability

Data will be made available on request.

Acknowledgments

This work was financially supported by the National Natural Science Foundation of China (52106144, 51922045, 52036003). We appreciate the support from the Analytical and Testing Center at Huazhong University of Science & Technology.

Appendix A. Supplementary material

Supplementary data associated with this article can be found in the online version at [doi:10.1016/j.apcatb.2022.122124](https://doi.org/10.1016/j.apcatb.2022.122124).

References

- [1] W. Wang, S.P. Wang, X.B. Ma, J.L. Gong, Recent advances in catalytic hydrogenation of carbon dioxide, *Chem. Soc. Rev.* 40 (2011) 3703–3727.
- [2] M. Aresta, A. Dibenedetto, E. Quaranta, State of the art and perspectives in catalytic processes for CO₂ conversion into chemicals and fuels: the distinctive contribution of chemical catalysis and biotechnology, *J. Catal.* 343 (2016) 2–45.
- [3] G.A. Olah, G.K.S. Prakash, A. Goepfert, Anthropogenic chemical carbon cycle for a sustainable future, *J. Am. Chem. Soc.* 133 (2011) 12881–12898.

- [4] S. Zhang, Q. Fan, R. Xia, T.J. Meyer, CO₂ reduction: from homogeneous to heterogeneous electrocatalysis, *Acc. Chem. Res.* 53 (2020) 255–264.
- [5] H.S. Shafaat, J.Y. Yang, Uniting biological and chemical strategies for selective CO₂ reduction, *Nat. Catal.* 4 (2021) 928–933.
- [6] C. Hepburn, E. Adlen, J. Beddington, E.A. Carter, S. Fuss, N. Mac Dowell, J.C. Minx, P. Smith, C.K. Williams, The technological and economic prospects for CO₂ utilization and removal, *Nature* 575 (2019) 87–97.
- [7] C. Weetman, P. Bag, T. Szilvasi, C. Jandl, S. Inoue, CO₂ fixation and catalytic reduction by a neutral aluminum double bond, *Angew. Chem. Int. Ed.* 58 (2019) 10961–10965.
- [8] Y.F. Zhao, G.I.N. Waterhouse, G.B. Chen, X.Y. Xiong, L.Z. Wu, C.H. Tung, T. R. Zhang, Two-dimensional-related catalytic materials for solar-driven conversion of CO_x into valuable chemical feedstocks, *Chem. Soc. Rev.* 48 (2019) 1972–2010.
- [9] S. Kar, A. Goepfert, G.K.S. Prakash, Integrated CO₂ capture and conversion to formate and methanol: connecting two threads, *Acc. Chem. Res.* 52 (2019) 2892–2903.
- [10] T. Schaub, CO₂-based hydrogen storage: CO₂ hydrogenation to formic acid, formaldehyde and methanol, *Phys. Sci. Rev.* 3 (2018).
- [11] Y.Q. Han, H.T. Xu, Y.Q. Su, Z.L. Xu, K.F. Wang, W.Z. Wang, Noble metal (Pt, Au@Pd) nanoparticles supported on metal organic framework (MOF-74) nanoshuttles as high-selectivity CO₂ conversion catalysts, *J. Catal.* 370 (2019) 70–78.
- [12] C.Q. Song, X. Liu, M. Xu, D. Masi, Y.G. Wang, Y.C. Deng, M.T. Zhang, X.T. Qin, K. Feng, J. Yan, J. Leng, Z.H. Wang, Y. Xu, B.H. Yan, S.Y. Jin, D.S. Xu, Z. Yin, D. Q. Xiao, D. Ma, Photothermal conversion of CO₂ with tunable selectivity using Fe-based catalysts: from oxide to carbide, *ACS Catal.* 10 (2020) 10364–10374.
- [13] L.X. Wang, E.J. Guan, Z.Q. Wang, L. Wang, Z.M. Gong, Y. Cui, Z.Y. Yang, C. T. Wang, J. Zhang, X.J. Meng, P.J. Hu, X.Q. Gong, B.C. Gates, F.S. Xiao, Dispersed nickel boosts catalysis by copper in CO₂ hydrogenation, *ACS Catal.* 10 (2020) 9261–9270.
- [14] I.A. Digdaya, I. Sullivan, M. Lin, L.H. Han, W.H. Cheng, H.A. Atwater, C.X. Xiang, A direct coupled electrochemical system for capture and conversion of CO₂ from oceanwater, *Nat. Commun.* 11 (2020).
- [15] Z. Jiang, X.H. Xu, Y.H. Ma, H.S. Cho, D. Ding, C. Wang, J. Wu, P. Oleynikov, M. Jia, J. Cheng, Y. Zhou, O. Terasaki, T.Y. Peng, L. Zan, H.X. Deng, Filling metal-organic framework mesopores with TiO₂ for CO₂ photoreduction, *Nature* 586 (2020) 549.
- [16] S. Kattel, B.H. Yan, J.G.G. Chen, P. Liu, CO₂ hydrogenation on Pt, PtSiO₂(2) and Pt/TiO₂: importance of synergy between Pt and oxide support, *J. Catal.* 343 (2016) 115–126.
- [17] J.A. Rodriguez, J. Evans, L. Feria, A.B. Vidal, P. Liu, K. Nakamura, F. Illas, CO₂ hydrogenation on Au/TiC, Cu/TiC, and Ni/TiC catalysts: production of CO, methanol, and methane, *J. Catal.* 307 (2013) 162–169.
- [18] Z.S. Shi, Q.Q. Tan, C. Tian, Y. Pan, X.W. Sun, J.X. Zhang, D.F. Wu, CO₂ hydrogenation to methanol over Cu-In intermetallic catalysts: effect of reduction temperature, *J. Catal.* 379 (2019) 78–89.
- [19] T. Avanesian, G.S. Gusmao, P. Christopher, Mechanism of CO₂ reduction by H₂ on Ru(0001) and general selectivity descriptors for late-transition metal catalysts, *J. Catal.* 343 (2016) 86–96.
- [20] J.A. Rodriguez, P. Liu, D.J. Stacchiola, S.D. Senanayake, M.G. White, J.G.G. Chen, Hydrogenation of CO₂ to methanol: importance of metal-oxide and metal-carbide interfaces in the activation of CO₂, *ACS Catal.* 5 (2015) 6696–6706.
- [21] J.R. Khushnudinova, J.A. Garg, D. Milstein, Combining low-pressure CO₂ capture and hydrogenation to form methanol, *ACS Catal.* 5 (2015) 2416–2422.
- [22] S.Q. Xie, W.L. Zhang, C.H. Jia, S.S.G. Ong, C. Zhang, S.C. Zhang, H.F. Lin, Eliminating carbon dioxide emissions at the source by the integration of carbon dioxide capture and utilization over noble metals in the liquid phase, *J. Catal.* 389 (2020) 247–258.
- [23] X. Jiang, X.W. Nie, X.X. Wang, H.Z. Wang, N. Koizumi, Y.G. Chen, X.W. Guo, C. S. Song, Origin of Pd-Cu bimetallic effect for synergetic promotion of methanol formation from CO₂ hydrogenation, *J. Catal.* 369 (2019) 21–32.
- [24] W. Zhang, X.L. Ma, H. Xiao, M. Lei, J. Li, Mechanistic investigations on thermal hydrogenation of CO₂ to methanol by nanostructured CeO₂(100): the crystal-plane effect on catalytic reactivity, *J. Phys. Chem. C* 123 (2019) 11763–11771.
- [25] P.P. Wu, B. Yang, Significance of surface formate coverage on the reaction kinetics of methanol synthesis from CO₂ hydrogenation over Cu, *ACS Catal.* 7 (2017) 7187–7195.
- [26] A.M. Bahmanpour, A. Hoadley, A. Tanksale, Critical review and exergy analysis of formaldehyde production processes, *Rev. Chem. Eng.* 30 (2014) 583–604.
- [27] L.E. Heim, H. Konnerth, M.H.G. Precht, Future perspectives for formaldehyde: pathways for reductive synthesis and energy storage, *Green Chem.* 19 (2017) 2347–2355.
- [28] L.E. Heim, H. Konnerth, M.H.G. Precht, The prospecting shortcut to an old molecule: formaldehyde synthesis at low temperature in solution, *ChemSusChem* 9 (2016) 2905–2907.
- [29] D.K. Lee, D.S. Kim, S.W. Kim, Selective formation of formaldehyde from carbon dioxide and hydrogen over PtCu/SiO₂, *Appl. Organomet. Chem.* 15 (2001) 148–150.
- [30] S. Careno, C.H. Wu, A. Shavorskiy, S. Alayoglu, G.A. Somorjai, H. Bluhm, M. Salmeron, Synthesis and structural evolution of nickel-cobalt nanoparticles under H₂ and CO₂, *Small* 11 (2015) 3045–3053.
- [31] A.M. Bahmanpour, A. Hoadley, A. Tanksale, Formaldehyde production via hydrogenation of carbon monoxide in the aqueous phase, *Green Chem.* 17 (2015) 3500–3507.
- [32] A.M. Bahmanpour, A. Hoadley, S.H. Mushrif, A. Tanksale, Hydrogenation of carbon monoxide into formaldehyde in liquid media, *ACS Sustain. Chem. Eng.* 4 (2016) 3970–3977.
- [33] F.L. Chan, G. Altinkaya, N. Fung, A. Tanksale, Low temperature hydrogenation of carbon dioxide into formaldehyde in liquid media, *Catal. Today* 309 (2018) 242–247.
- [34] J.W. Zhao, S. Xu, H.J. Wu, Z.X. You, L.D. Deng, X.H. Qiu, Metal-support interactions on Ru/CaAlO_x catalysts derived from structural reconstruction of Ca-Al layered double hydroxides for ammonia decomposition, *Chem. Commun.* 55 (2019) 14410–14413.
- [35] Z.Z. Yang, J.J. Wei, G.M. Zeng, H.Q. Zhang, X.F. Tan, C. Ma, X.C. Li, Z.H. Li, C. Zhang, A review on strategies to LDH-based materials to improve adsorption capacity and photoreduction efficiency for CO₂, *Coord. Chem. Rev.* 386 (2019) 154–182.
- [36] N. Dewangan, W.M. Hui, S. Jayaprakash, A.R. Bawah, A.J. Poerjoto, T. Jie, A. Jangam, K. Hidayat, S. Kawi, Recent progress on layered double hydroxide (LDH) derived metal-based catalysts for CO₂ conversion to valuable chemicals, *Catal. Today* 356 (2020) 490–513.
- [37] M.G. Veerabhadrapa, M.M. Maroto-Valer, Y.H. Chen, S. Garcia, Layered double hydroxides-based mixed metal oxides: development of novel structured sorbents for CO₂ capture applications, *ACS Appl. Mater. Interfaces* 13 (2021) 11805–11813.
- [38] X. Fang, C. Chen, H. Jia, Y.N. Li, J. Liu, Y.S. Wang, Y.L. Song, T. Du, L.Y. Liu, Progress in adsorption-enhanced hydrogenation of CO₂ on layered double hydroxide (LDH) derived catalysts, *J. Ind. Eng. Chem.* 95 (2021) 16–27.
- [39] J. Dou, Y. Sheng, C. Choong, L.W. Chen, H.C. Zeng, Silica nanowires encapsulated Ru nanoparticles as stable nanocatalysts for selective hydrogenation of CO₂ to CO, *Appl. Catal. B Environ.* 219 (2017) 580–591.
- [40] R. Mutschler, E. Moio, W. Luo, N. Galland, A. Züttel, CO₂ hydrogenation reaction over pristine Fe, Co, Ni, Cu and Al₂O₃ supported Ru: comparison and determination of the activation energies, *J. Catal.* 366 (2018) 139–149.
- [41] F.J. Quan, G.M. Zhan, C.L. Mao, Z.H. Ai, F.L. Jia, L.Z. Zhang, H.G. Gu, S.Y. Liu, Efficient light-driven CO₂ hydrogenation on Ru/CeO₂ catalysts, *Catal. Sci. Technol.* 8 (2018) 6503–6510.
- [42] W.J. Zhang, S.P. Wang, Y.J. Zhao, X.B. Ma, Hydrogenation of CO₂ to formic acid catalyzed by heterogeneous Ru-PPh₃/Al₂O₃ catalysts, *Fuel Process Technol.* 178 (2018) 8–103.
- [43] B.F. Chen, M.H. Dong, S.L. Liu, Z.B. Xie, J.J. Yang, S.P. Li, Y.Y. Wang, J. Du, H. Z. Liu, B.X. Han, CO₂ hydrogenation to formate catalyzed by Ru coordinated with a N,P-containing polymer, *ACS Catal.* 10 (2020) 8557–8566.
- [44] C.L. Mathis, J. Geary, Y. Ardon, M.S. Reese, M.A. Philliber, R.T. VanderLinden, C. T. Sauma, Thermodynamic analysis of metal-ligand cooperativity of PNP Ru complexes: implications for CO₂ hydrogenation to methanol and catalyst inhibition, *J. Am. Chem. Soc.* 141 (2019) 14317–14328.
- [45] Y. Tokudome, M. Fukui, S. Iguchi, Y. Hasegawa, K. Teramura, T. Tanaka, M. Takemoto, R. Katsura, M. Takahashi, A nanoLDH catalyst with high CO₂ adsorption capability for photo-catalytic reduction, *J. Mater. Chem. A* 6 (2018) 9684–9690.
- [46] S.Y. Jung, B.K. Kim, S. Hirata, M. Inada, J.M. Oh, Particle size effect of layered double hydroxide on the porosity of calcined metal oxide, *Appl. Clay Sci.* 195 (2020).
- [47] J. Rocha, M. del Arco, V. Rives, M.A. Ulibarri, Reconstruction of layered double hydroxides from calcined precursors: a powder XRD and Al-27 MAS NMR study, *J. Mater. Chem.* 9 (1999) 2499–2503.
- [48] K. Takehira, Recent development of layered double hydroxide-derived catalysts - rehydration, reconstitution, and supporting, aiming at commercial application, *Appl. Catal. Sci.* 136 (2017) 112–141.
- [49] M. Thommes, K. Kaneko, A.V. Neimark, J.P. Olivier, F. Rodriguez-Reinoso, J. Rouquerol, K.S.W. Sing, Physisorption of gases, with special reference to the evaluation of surface area and pore size distribution (IUPAC Technical Report), *Pure Appl. Chem.* 87 (2015) 1051–1069.
- [50] B.S. Marques, K. Dalmagro, K.S. Moreira, M.L.S. Oliveira, S.L. Jahn, T.A.D. Burgo, G.L. Dotto, Ca-Al, Ni-Al and Zn-Al LDH powders as efficient materials to treat synthetic effluents containing o-nitrophenol, *J. Alloy Compd.* 838 (2020).
- [51] A. Fahami, E.S.M. Duraia, G.W. Beall, M. Fahami, Facile synthesis and structural insight of chloride intercalated Ca/Al layered double hydroxide nanopowders, *J. Alloy Compd.* 727 (2017) 970–977.
- [52] C.H. Wu, Y.P. Chang, S.Y. Chen, D.M. Liu, C.T. Yu, B.L. Pen, Characterization and structure evolution of Ca-Al-CO₃ hydrothermal film for high temperature CO₂ adsorption, *J. Nanosci. Nanotechnol.* 10 (2010) 4716–4720.
- [53] X. Wang, L. Pan, K.Q. Wu, L.L. Li, J.Y. Xu, H.C. Lau, Experiment based modeling of CO₂ solubility in H₂O at 313.15–473.15 K and 0.5–200 MPa, *Appl. Geochem.* 130 (2021).
- [54] L. Deng, X. Liu, J. Xu, Z. Zhou, S. Feng, Z. Wang, M. Xu, Transfer hydrogenation of CO₂ into formaldehyde from aqueous glycerol heterogeneously catalyzed by Ru bound to LDH, *Chem. Commun.* 57 (2021) 5167–5170.
- [55] I. Lavilla, N. Cabaleiro, F. Pena, I. de la Calle, C. Bendicho, Ultrasound-assisted emulsification microextraction with simultaneous derivatization coupled to fibre optics-based cuvetteless UV-vis micro-spectrophotometry for formaldehyde determination in cosmetic samples, *Anal. Chim. Acta* 674 (2010) 59–63.
- [56] I.J. Boyer, B. Heldreth, W.F. Bergfeld, D.V. Belsito, R.A. Hill, C.D. Klaassen, D. C. Lieber, J.G. Marks, R.C. Shank, T.J. Slaga, P.W. Snyder, F.A. Andersen, Amended safety assessment of formaldehyde and methylene glycol as used in cosmetics, *Int. J. Toxicol.* 32 (2013) 58–325.
- [57] J.G.M. Winkelman, M. Ottens, A.A.C.M. Beenackers, The kinetics of the dehydration of methylene glycol, *Chem. Eng. Sci.* 55 (2000) 2065–2071.
- [58] J.G.M. Winkelman, O.K. Voorwinde, M. Ottens, A.A.C.M. Beenackers, L.P.B. M. Janssen, Kinetics and chemical equilibrium of the hydration of formaldehyde, *Chem. Eng. Sci.* 57 (2002) 4067–4076.

- [59] J.K. Norskov, T. Bligaard, B. Hvolbaek, F. Abild-Pedersen, I. Chorkendorff, C. H. Christensen, The nature of the active site in heterogeneous metal catalysis, *Chem. Soc. Rev.* 37 (2008) 2163–2171.
- [60] L.D. Deng, H. Miura, T. Shishido, Z. Wang, S. Hosokawa, K. Teramura, T. Tanaka, Elucidating strong metal-support interactions in Pt-Sn/SiO₂ catalyst and its consequences for dehydrogenation of lower alkanes, *J. Catal.* 365 (2018) 277–291.
- [61] F. Zaera, Nanostructured materials for applications in heterogeneous catalysis, *Chem. Soc. Rev.* 42 (2013) 2746–2762.
- [62] K. Zhao, L.G. Wang, E. Moiola, M. Calizzi, A. Zuttel, Identifying reaction species by evolutionary fitting and kinetic analysis: an example of CO₂ hydrogenation in DRIFTS, *J. Phys. Chem. C* 123 (2019) 8785–8792.
- [63] A. Sapi, G. Halasi, J. Kiss, D.G. Dobo, K.L. Juhasz, V.J. Kolcsar, Z. Ferencz, G. Vari, V. Matolin, A. Erdohelyi, A. Kukovecz, Z. Konya, In Situ DRIFTS and NAP-XPS exploration of the complexity of CO₂ hydrogenation over size-controlled Pt nanoparticles supported on mesoporous NiO, *J. Phys. Chem. C* 122 (2018) 5553–5565.
- [64] L. Proano, E. Tello, M.A. Arellano-Trevino, S.X. Wang, R.J. Farrauto, M. Cobo, In-situ DRIFTS study of two-step CO₂ capture and catalytic methanation over Ru,"Na₂O"/Al₂O₃ dual functional material, *Appl. Surf. Sci.* 479 (2019) 25–30.
- [65] A. Cardenas-Arenas, A. Quindimil, A. Davo-Quinonero, E. Bailon-Garcia, D. Lozano-Castello, U. De-La-Torre, B. Pereda-Ayo, J.A. Gonzalez-Marcos, J. R. Gonzalez-Velasco, A. Bueno-Lopez, Isotopic and in situ DRIFTS study of the CO₂ methanation mechanism using Ni/CeO₂ and Ni/Al₂O₃ catalysts, *Appl. Catal. B Environ.* 265 (2020).
- [66] M. Bersani, K. Gupta, A.K. Mishra, R. Lanza, S.F.R. Taylor, H.U. Islam, N. Hollingsworth, C. Hardacre, N.H. de Leeuw, J.A. Darr, Combined EXAFS, XRD, DRIFTS, and DFT study of nano copper based catalysts for CO₂ hydrogenation, *ACS Catal.* 6 (2016) 5823–5833.
- [67] H.J. Wu, M.W. Yuan, J. Huang, X.Z. Li, Y. Wang, J.J. Li, Z.X. You, CO₂ methanation over Ru/12CaO center dot 7Al₍₂₃₎O₍₃₎ catalysts: effect of encaged anions on catalytic mechanism, *Appl. Catal. A Gen.* 595 (2020).
- [68] X.Y. Chen, G.Z. He, Y.B. Li, M. Chen, X.X. Qin, C.B. Zhang, H. He, Identification of a facile pathway for dioxymethylene conversion to formate catalyzed by surface hydroxyl on TiO₂-based catalyst, *ACS Catal.* 10 (2020) 9706–9715.
- [69] X.Y. Liu, P. Schlexer, J.P. Xiao, Y.F. Ji, L. Wang, R.B. Sandberg, M. Tang, K. S. Brown, H.J. Peng, S. Ringe, C. Hahn, T.F. Jaramillo, J.K. Norskov, K.R. Chan, pH effects on the electrochemical reduction of CO₂ towards C₂ products on stepped copper, *Nat. Commun.* 10 (2019).
- [70] P. Zhao, Y.R. He, D.B. Cao, X.D. Wen, H.W. Xiang, Y.W. Li, J.G. Wang, H.J. Jiao, High coverage adsorption and co-adsorption of CO and H₂ on Ru(0001) from DFT and thermodynamics, *Phys. Chem. Chem. Phys.* 17 (2015) 19446–19456.
- [71] W. Zhang, M. Pu, M. Lei, Theoretical studies on the stability and reactivity of the metal-doped CeO₂ (100) surface: toward H₂ dissociation and oxygen vacancy formation, *Langmuir* 36 (2020) 5891–5901.
- [72] T.J. Schmeier, G.E. Dobereiner, R.H. Crabtree, N. Hazari, Secondary coordination sphere interactions facilitate the insertion step in an iridium(III) CO₂ reduction catalyst, *J. Am. Chem. Soc.* 133 (2011) 9274–9277.
- [73] Y. Himeda, N. Onozawa-Komatsuzaki, H. Sugihara, K. Kasuga, Simultaneous tuning of activity and water solubility of complex catalysts by acid-base equilibrium of ligands for conversion of carbon dioxide, *Organometallics* 26 (2007) 702–712.